Int. J. Electrochem. Sci., 16 **(2021)** Article ID: 210836, doi: 10.20964/2021.08.05

International Journal of
ELECTROCHEMICAL
SCIENCE
www.electrochemsci.org

Silicon/Spent Coffee Waste-derived Carbon Composite as an Efficient Anode for Li-ion Batteries

Nulu Venugopal

Department of Nanoscience and Engineering, Center for Nano Manufacturing, Inje University, 197 Inje-ro, Gimhae, Gyeongnam-do 50834, Republic of Korea
E-mail: venungopal@inje.ac.kr; venungopal@gmail.com

Received: 23 March 2021 / *Accepted:* 18 May 2021 / *Published:* 30 June 2021

Silicon anodes are the most investigated materials for Li-ion batteries (LIBs) owing to their high theoretical capacity and low working potential. However, significant volume changes and low conductivity hinder their practical applications. The addition of carbon and the formation of a silicon/carbon composite are established paths for improving the structural stability and conductivity of silicon anodes. In this study, spent coffee waste (SCW) was chosen as an eco-friendly and cost-effective carbon source for fabricating a composite with silicon. The prepared Si and SCW-derived activated carbon (SCWAC) composite was studied as an anode for Li-ion batteries. The composite exhibited improved electrochemical performance compared to bare silicon nanoparticles. The noticeable improvement could be attributed to the structural stability and conductivity provided by the SCWAC matrix. The proposed composite delivered a discharge capacity of 1122 mAh g^{-1} after 100 cycles at a current density of 200 mA g^{-1}. The composite also showed better Li^+ diffusion properties, which enhanced the Li^+-ion storage capability. This work contributes to the development of eco-environmental batteries using low-cost materials, as a promising solution to address increasing energy storage demands.

Keywords: coffee waste-derived carbon, silicon-carbon composite, anode material, li-ion diffusion, li-ion batteries

1. INTRODUCTION

The tremendous increase in the demand for high energy requires the development of advanced energy storage devices capable of delivering high energy and power densities with safe, environmentally friendly, and inexpensive components [1-3]. For the past few decades, lithium-ion batteries (LIBs) have cornered the energy storage market owing to their high energy density, long-term stability, and low self-discharge rates [4,5]. Electrode materials with high specific capacity and good structural/mechanical stability are required to achieve high energy and power densities. Currently, graphite (theoretical capacity 372 mAh g^{-1}) is used as a conventional anode material for LIBs, but may not be sufficient to

meet the demands of existing high-energy and high-power applications. From this perspective, silicon, with a high theoretical capacity of 3590 mAh g^{-1} and low working potential of ~0.4 V vs. Li/Li^+, has attracted the attention of researchers. Its abundance in the earth's crust and its eco-friendly nature further encourage its practical application as an anode material [6,7]. However, the alloying/dealloying reactions of Li^+ ions promote massive volume changes and cracking in Si, leading to the formation of an unstable solid electrolyte interphase (SEI) layer, which eventually causes a rapid decline in the specific capacity. The low intrinsic conductivity and lack of structural stability further hamper the overall battery performance [8,9]. A few previous reports have revealed that internal cracking, pulverization, and unstable SEI formation are critical factors that accelerate deterioration of the battery performance [10,11]. Comprehensive approaches have been developed to overcome the drawbacks of Si-based electrodes, such as volume changes and low electronic conductivity. The size of the Si particles plays an important role in their performance as anode materials. Reducing the Si particle size from bulk to nano dimensions can effectively control the structural damage and provide a large surface area, which can increase the contact area of the electrolyte with the active material for Li^+ ion reactions and improve the cycling performance [12-14]. The preparation of carbon-coated nano-silicon or fabrication of Si and carbon composites can effectively overcome the limitations of Si anodes. Composite formation with carbon prevents the drawbacks associated with bare silicon anode materials, such as the large volume changes that occur during charge-discharge cycling, by providing the required buffering volume and augmenting the electrical conductivity of the composite electrode [15-17]. Different carbon sources such as polyvinyl pyrrolidone, citric acid, gelatin, polyvinyl alcohol, polyacrylonitrile, and polyvinylidene fluoride have been used as precursors to make carbon coatings or composites with Si particles [18-22]. All these carbon sources are unsafe and require time-intensive and multi-step reaction procedures. Using biomass carbon sources effectively controls the production cost of the active materials for energy storage applications. Indeed, various biomass-derived carbons, such as carbons derived from mushrooms, rice husks, and sweet potatoes, have been used as efficient anode materials for LIBs owing to their suitable structures, easy availability, and cost-effective source materials [23-26].

From this perspective, spent coffee waste (SCW) attracted our attention because SWC constitutes 90% of the coffee produced [27]. SCW is rich in carbon and can be utilized as an effective source of pyrolytic carbon and represents a strong biomass resource. Several applications of SCW-derived carbon have been reported, such as biochar-derived adsorbents [28], bioactive compounds [29], methane storage [30], and hierarchically porous carbon powders/nanosheets for energy storage applications such as supercapacitors, Na-ion batteries, and LIBs [31-33]. To date, there have been no reports on SCW-derived carbon composites with Si. To exploit its advantages, SCW is used herein as a low-cost carbon source for fabricating Si/carbon composites as an advanced anode material for achieving improved lithium-ion battery performance. A traditional KOH-mediated approach is employed to obtain activated carbon (AC) from SCW. The prepared AC material is used to form a composite with Si nanoparticles. As expected, the prepared Si/carbon composite exhibits improved electrochemical properties compared to the pristine Si nanoparticles.

2. EXPERIMENTAL

2.1 Material Synthesis

Preparation of AC: AC was prepared from SCW according to a previously reported procedure [34]. The step-by-step preparation of AC is illustrated in Fig. 1a. The SCW was collected from the university coffee shop, washed with water to remove impurities and water-soluble substances, dried overnight in a vacuum oven at 100 °C, and sieved with a 100 µm mesh to separate the larger particles. SCW fine powder (10.0 g) was mixed with KOH (Sigma Aldrich) (SCW/KOH = 1:2 ratio) and ground well with a mortar and pestle to form a homogeneous mixture. The mixture was calcined in a tube furnace under an Ar atmosphere at 700 °C for 3 h at a heating rate of 5 °C min^{-1}. After calcination, the obtained solid was washed well with 1 M HCl (Sigma Aldrich) to remove excess KOH. Thereafter, the obtained material was washed with distilled water, dried overnight in an oven at 80 °C, and stored for further analysis.

Preparation of Si/SCWAC composite: A schematic of the preparation of the Si/SCWAC composite is shown in Fig. 1b. The Si nanoparticles (0.7 wt%; < 50 nm; Alfa Aesar) were combined with 0.3 wt% of AC powder in the zirconium bowl of a mini-mill. A few drops of ethanol were added to the powders. The lid was closed, and all the components were mixed well at a speed of 30 oscillations per second for 1 h to make a uniform slurry. The obtained slurry was heat-treated in a tube furnace at 400 °C for 1 h under argon atmosphere. After heating, the furnace was cooled to room temperature; the collected product is hereafter termed the Si/SCWAC composite.

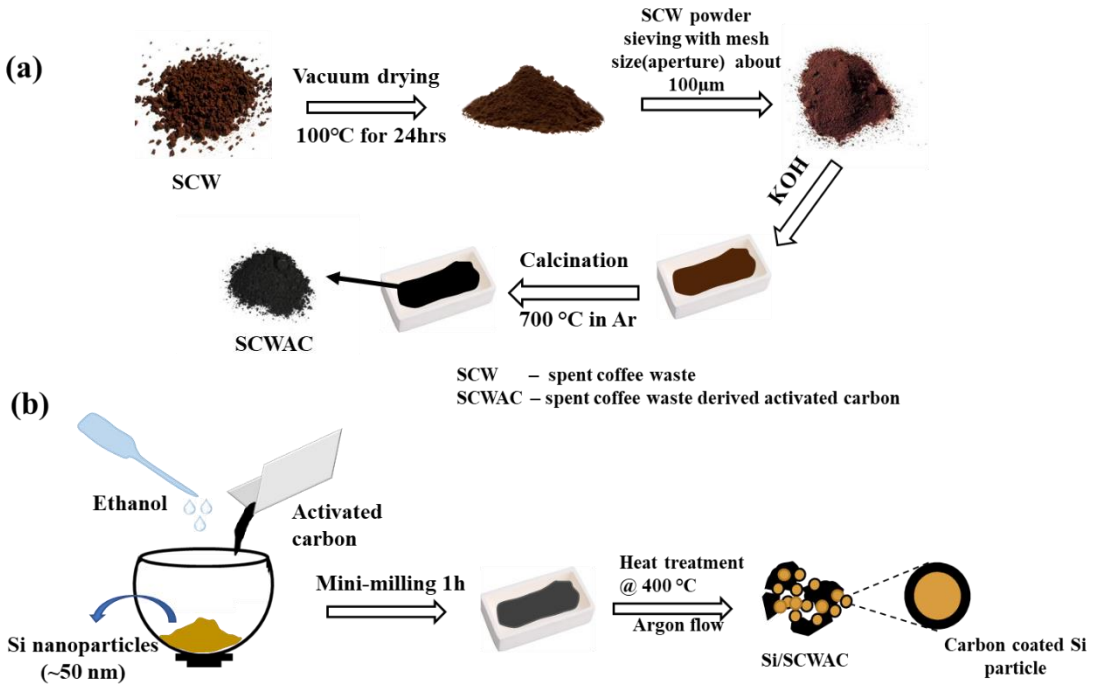

Figure 1. (a) Schematic of preparation of activated carbon. (b) Step-by-step fabrication of Si/SCWAC composite.

2.2 Characterization

The crystallographic structure of the prepared material was determined by X-ray diffraction (XRD) in the range of $10° < 2\theta < 80°$. Raman spectroscopy was used to analyze the carbon content. The surface morphologies of the materials were studied using scanning electron microscopy (SEM) and transmission electron microscopy (TEM). Thermogravimetric analysis (TGA) data were recorded at 50–800 °C at a heating rate of 10 °C min^{-1} under air atmosphere.

2.3 Electrochemical measurements

All electrochemical measurements were performed using 2032R button-type coin cells. The working electrodes were prepared from 70 wt% of the active material with 20 wt% super P and 10 wt% polyvinylidene fluoride (PVDF) in *N*-methyl pyrrolidone (NMP) solution. All added components were mixed well using a mini-mill for 30 min to obtain a homogeneous slurry. The resulting slurry was uniformly cast on a copper foil using the traditional doctor blade method. The electrode was dried at 80 °C for 2 h to evaporate the NMP. The dry electrode was placed in a vacuum oven and heated at 200 °C for 3 h. The bare Si NP electrode was separately prepared under the same conditions for comparison with the Si/SCWAC composite electrode. All prepared electrodes were punched with a diameter of 14 mm. The calculated mass loading of the active material on the copper foil was ~1.1 mg cm^{-2}, with an average thickness of 85 μm. All cells were fabricated in an argon-filled glove box, using metallic Li as the counter electrode, a polypropylene membrane as the separator, and 1 M $LiPF_6$ in ethylene carbonate, diethyl carbonate, and fluoroethylene carbonate (v/v ratio of 5/70/25) as the electrolyte. All cells were examined in the voltage window of 0.01–2.0 V vs. Li/Li^+ at an applied current density of 200 mA g^{-1}. Rate capability tests were performed over a wide range of current densities (100–3200 mA g^{-1}). The redox behavior was analyzed using cyclic voltammetry (CV) in the voltage range of 0.01–2.0 V at 0.1 mV s^{-1} scan rate. Electrochemical impedance spectroscopy (EIS) studies were performed in the frequency range of 10 Hz –10 kHz to evaluate the reaction kinetics of the composite material.

3. RESULTS AND DISCUSSION

The XRD patterns of the prepared SCWAC and Si/SCWAC composites are shown in Fig. 2a and b. Figure 2a shows two characteristic peaks at ~24.5° and 43.2°, which correspond to the (002) and (100) crystal planes of AC derived from SCW, and are related to the layered carbon structure and hexagonal sp^2 hybridized carbon structures, respectively [32]. The XRD patterns of the bare Si nanoparticles and Si/SCWAC composites are shown in Fig. 2b. The main diffraction peaks at 2θ = 28.4°, 47.4°, 56.2°, 69.2°, and 79.5° (JCPDS#27- 1402) for the Si/SCWAC composite (Fig. 2b) correspond to the (111), (220), (311), (400), and (331) lattice planes of crystalline Si, indicating that the crystalline nature of Si was well-retained after heat treatment. The broad peak at 2θ = 20–25° corresponds to the combination of amorphous SiO_x and SCWAC. Here, SiO_x could be formed during the heating process because of the highly reactive surface of the Si NPs [16-17]. The amount of carbon in the composite was determined

using TGA. The TGA curves for the Si NPs and Si/SCWAC composite samples were measured in the range of 50–800 °C at a heating rate of 10 °C min^{-1} under air atmosphere (Fig. 2c). No weight loss was observed for the Si NPs, whereas above 500 °C, the slight weight increase demonstrates the formation of SiO_x owing to partial oxidation of the Si particles [35]. The calculated weight loss of the Si/SCWAC composite was 23.5%. Note that the AC content in the composite was lower than the actual weight added in the experiment, where this difference may be due to the loss of material during transfer of the sample to the crucible during the heating process [15]. The Raman spectra of the bare Si NPs and the prepared Si/C composite were analyzed within the range of 200–1200 cm^{-1} at room temperature, as shown in Fig. 2(d). Both samples exhibited characteristic peaks at 512 cm^{-1} and 933 cm^{-1}, indicative of crystalline Si. Two broad peaks were observed at 1340 and 1575 cm^{-1} in the profile of the Si/SCWAC composite, corresponding to the D and G bands, respectively, which are attributed to the structural defects and graphitic carbon, respectively. The nature of carbon in the composite can be predicted from the intensity ratio of the D and G bands (I_D/I_G). From the spectra, I_D/I_G was quantified as approximately 0.98, demonstrating that the carbon has highly graphitic characteristics and can confer excellent electrical conductivity to the composite material, leading to fast electron transport during the Li^+ ion charge/discharge reactions.

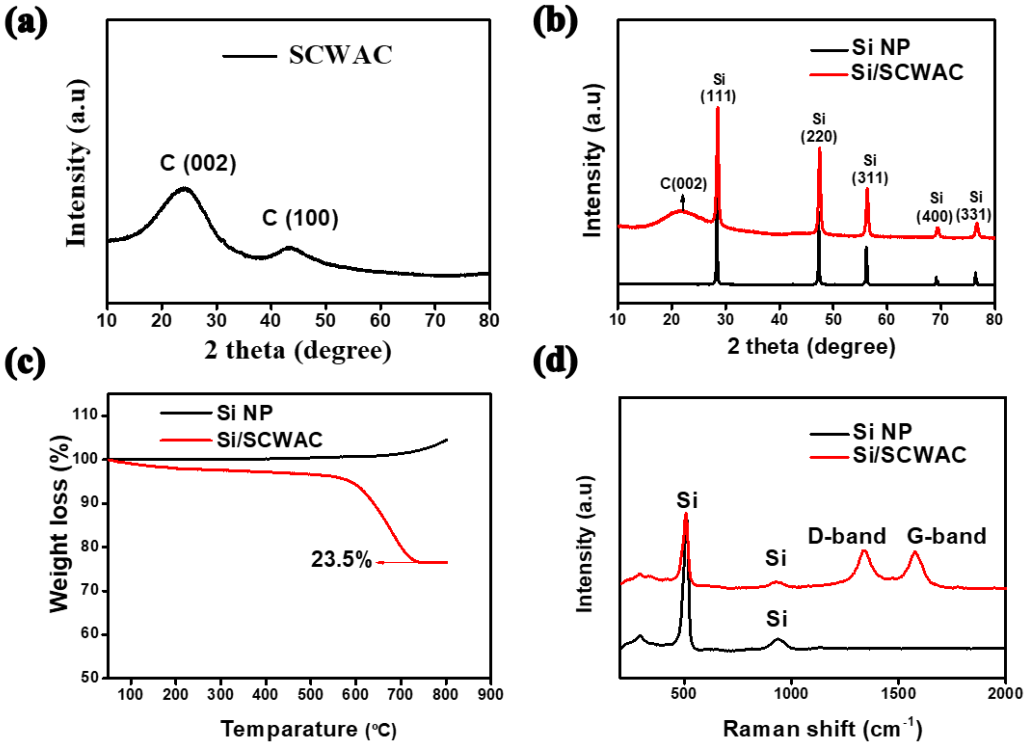

Figure 2. XRD patterns of (a) activated carbon derived from SCW, (b) bare Si and Si/SCWAC composite, (c) thermogravimetric analysis results, (d) Raman spectra of bare Si and Si/SCWAC composite.

The morphology of the prepared Si/SCWAC composite was investigated using SEM and TEM. Figure 3a shows the SEM image of the Si/SCWAC composite, demonstrating the aggregated morphology of the Si particles. The TEM images at different magnifications are shown in Fig. 3b and c, indicating that the Si nanoparticles were embedded in the carbon matrix, and some of them were coated with carbon (indicated by yellow arrows). Figure 3d shows a high-resolution TEM image of specific Si nanoparticles revealing the crystalline nature, with a d-spacing of 0.31 nm that matches the (111) plane of Si. The outer layer of Si was coated with an amorphous carbon layer, as indicated by the black arrow. The elemental distributions of the Si/SCWAC composite material were determined by energy-dispersive X-ray elemental mapping studies (Fig. 3e). The Si NPs (blue) were surrounded by a surface oxidation layer (red) combined with the carbon matrix (yellow), indicating successful formation of the Si/SCWAC composite, which is in good agreement with the XRD results.

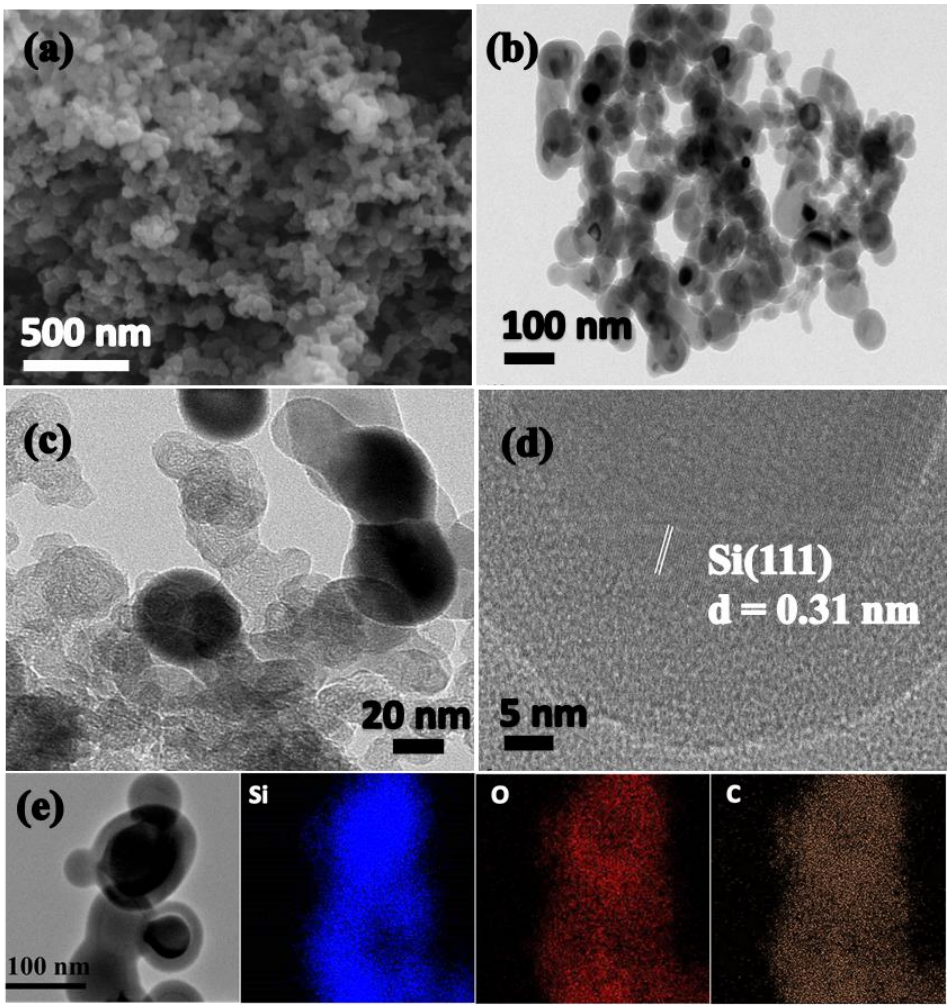

Figure 3. (a) SEM image, (b) and (c) TEM images, (d) HR-TEM image, (e) EDX- elemental mapping of Si/SCWAC composite.

Different electrochemical tests were conducted to evaluate the electrochemical properties of the prepared composite for use as an anode material. The redox behavior of the Si NPs and the prepared electrode was evaluated by cyclic voltammetry (CV) measurements at a scan rate of 0.1 mV s^{-1} within the voltage range of 0.01–2.0 V; the profiles of the first five CV cycles are shown in Fig. 4a and b, respectively. In the first lithiation of the cathodic scan, a broad reduction peak was observed at 1.2–0.4 V for the Si NPs, resulting from decomposition of the electrolyte and formation of the SEI layer on the electrode surface. However, for the Si/SCWAC composite, a distinct broad peak was observed around 0.65 V, indicating a greater extent of SEI layer formation. A possible reason for this larger SEI layer in the Si/SCWAC electrode is the availability of a much larger surface area due to the AC matrix, which is derived from the SCW. As a result, the prepared composite had a much higher electrolyte/electrode interfacial area to promote decomposition of the electrolyte and SEI layer formation. This peak disappeared in the following cycles for both electrodes, indicating the formation of a stable SEI layer [36]. The two other sharp peaks at ~0.14 V (for the Si NPs) and ~0.19 V (for the Si/SCWAC composite), at ~0.05 V vs. Li/Li^+, observed for both electrodes, are correlated to the alloying of Li^+ into crystalline Si and the formation of metastable amorphous Li_xSi phases.

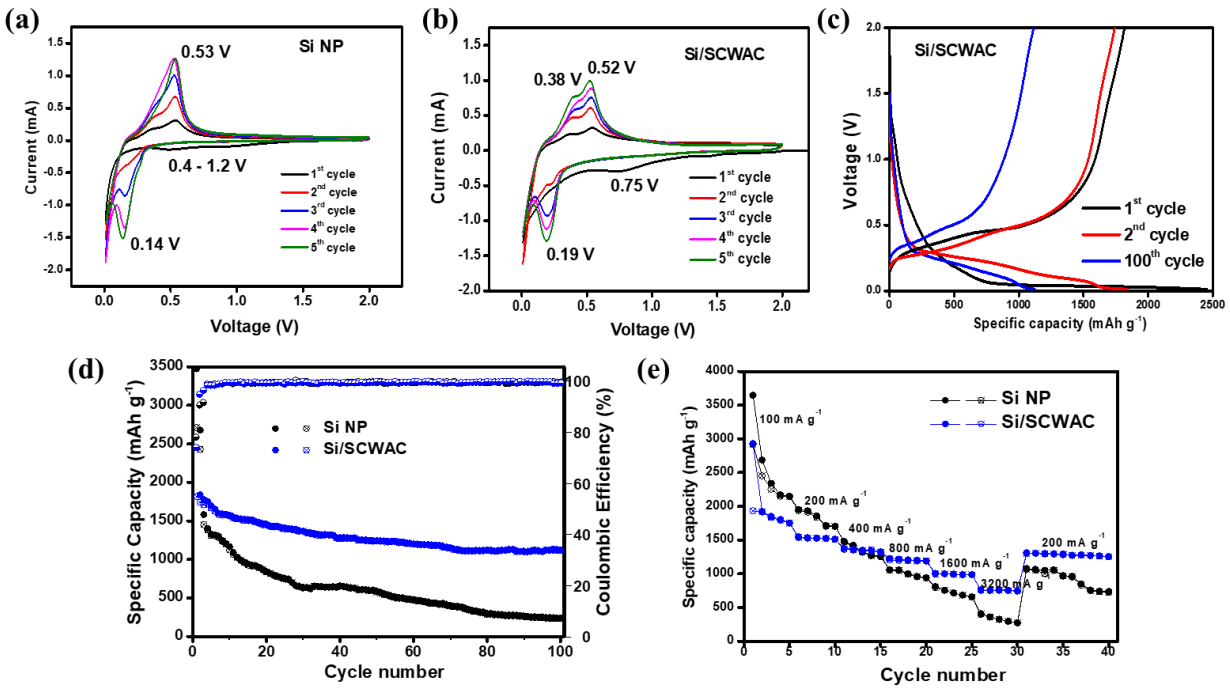

Figure 4. Cyclic voltammograms of (a) bare Si, (b) Si/SCWAC composite, (c) charge-discharge voltage profiles of Si/SCWAC composite, (d) cyclability with coulombic efficiency, (e) rate capability data for bare Si and Si/SCWAC composite.

The peaks at ~0.38 V and ~0.52 V vs. Li/Li^+ in the anodic scan for the Si/SCWAC composite are the typical peaks of the two-step dealloying of the Li_xSi phase to form amorphous Si. On the other hand, the profile of the Si NPs exhibited one anodic peak at 0.53 V vs. Li/Li^+, indicating the slow dealloying process. The CV curve reveals that the oxidation peak shifted to lower voltage, whereas the reduction peak shifted towards higher voltage for the composite compared with the Si NPs, which may

be due to the presence of the AC matrix, which leads to improved wetting and enhances the Li-ion insertion kinetics [36-38]. The increased sharpness of the peak and higher intensity in the following cycles indicate activation of the anode and excellent electrochemical reversibility [15,16].

The voltage vs. specific capacity plots of the Si/C composite for the 1st, 2nd, and 100th cycles at an applied current density of 200 mA g^{-1} are shown in Fig. 4c. The long discharge plateau below 0.1 V corresponds to the alloying of crystalline Si with lithium and the development of the Li_xSi phase. In the charging cycle, the plateau above 0.5 V corresponds to the dealloying of Li_xSi into amorphous Si. In the subsequent cycles, the discharge plateau shifted to 0.25 V because of the typical phase transformation of Si from crystalline to amorphous [39]. The composite electrode exhibited specific capacities of 2451/1815 mAh g^{-1} with a coulombic efficiency of 74%. The irreversible capacity loss of 636 mAh g^{-1} can be ascribed to decomposition the electrolyte and formation of the SEI layer on the surface of the electrode. In the 2nd cycle, the composite electrode exhibited a Coulombic efficiency of 94.8% with specific capacities of 1838/1742 mAh g^{-1}. The greater enhancement in the coulombic efficiency represents the formation of a stable SEI layer, and at the 100th cycle, the CE reached 99.3%. The cyclability results and CE data for the Si NPs and Si/SCWAC composites up to 100 cycles at 200 mA g^{-1} are displayed in Fig. 4d. The Si NPs initially displayed higher specific capacity, but with increasing cycle numbers, the capacity gradually decreased and reached 239/230 mAh g^{-1} after 100 cycles. The rapid capacity loss is related to the large volume changes of the active material during the Li^+ reactions, leading to loss of contact between the active material and the current collector. In contrast, the Si/SCWAC composite exhibited specific capacities of 1122/1115 mAh g^{-1} at the 100th cycle, where this excellent reversibility is attributed to the highly conductive, structurally stable AC matrix in the composite material. To further illustrate the excellent structural stability of the Si/C composite electrode, rate capability tests were carried out from 100 to 3200 mA g^{-1}; the corresponding specific capacity vs. cycle number plot is presented in Fig. 4e. The results show that the Si/C composite delivered excellent rate capability compared to the bare Si NPs. The composite electrode exhibited capacities of 2931, 1546, 1375, 1225, 1006, and 759 mAh g^{-1} at current densities of 100, 200, 400, 800, 1600, and 3200 mA g^{-1}, respectively. After applying a high current density of 3200 mAg^{-1}, the composite electrode retained a capacity of 1309 mAh g^{-1} at 200 mAg^{-1}, which is four-fold greater than that of a commercial graphite anode. However, in the case of Si NPs, the rate capability declined rapidly with increasing current density and reached 410 mAh g^{-1} at 3200 mAg^{-1}, which is much lower than that of Si/SCWAC. These results indicate that the AC matrix in the composite material crucially influences the structural stability, electrical conductivity, and buffer volume, leading to stability even at high applied current densities [40,41].

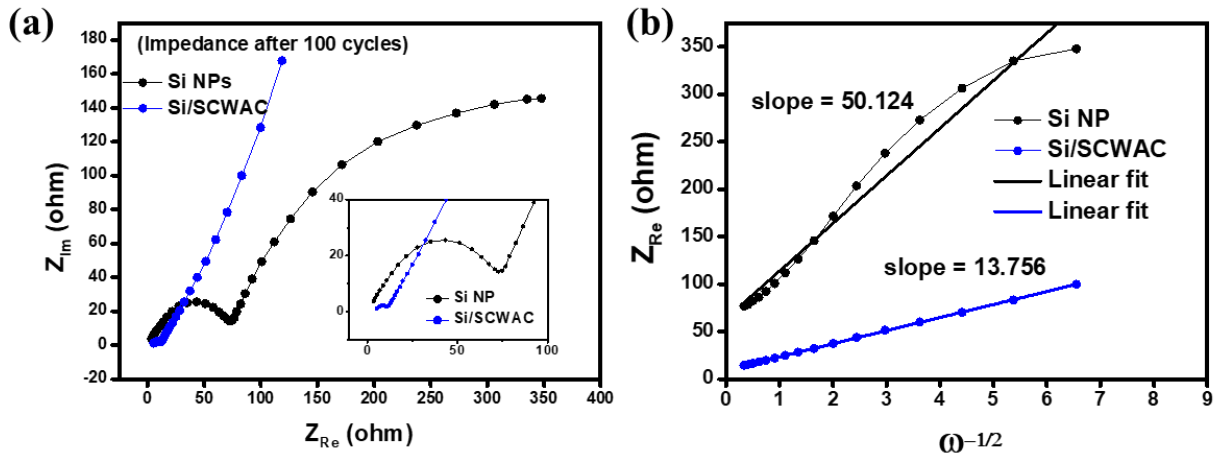

Figure 5. (a) Nyquist plots of bare Si and Si/SCWAC composite after 100 cycles, (b) fitting results of Z_{Re} versus $\omega^{-1/2}$ plots for bare Si and Si/SCWAC composite.

To further investigate the kinetics of the prepared Si/SCWAC composite electrode, the electrodes were subjected to EIS analysis after 100 charge/discharge cycles (Fig. 5a). The Nyquist plots of both electrodes exhibited depressed semicircles in the high-and middle-frequency regions and a straight line in the low-frequency region, associated with the charge transfer resistance at the electrode/electrolyte interface and the diffusion of Li^+ ions, respectively [42,43]. The diameter of the semicircle for the Si/SCWAC composite was much smaller than that of the Si NPs. The solution resistance (R_s) of the Si/SCWAC composite was quantified as 1.15 Ω, and the charge transfer resistance (R_{ct}) was 12 Ω, compared to the R_s of 3.55 Ω and R_{ct} of 81 Ω for the bare Si NPs. These results demonstrate that the AC matrix derived from SCW successfully afforded the required electron and ion channels and encouraged faster Li^+ ion diffusion during the alloying and dealloying process. The Z_{Re} vs. $\omega^{-1/2}$ plots of both the Si NPs and Si/SCWAC composite electrodes are shown in Fig. 5b, where Z_{Re} linearly depends on $\omega^{-1/2}$ in the low-frequency region. The equations below were used to estimate the diffusion coefficient of Li^+(D).

$$Z_{Re} = R_s + R_{ct} + \sigma_w \omega^{-1/2} \quad \text{Eq. (1)}$$

$$D = R^2 T^2 / 2A^2 F^4 C^2 \sigma_w^2 \quad \text{Eq. (2)}$$

Here, R is the gas constant, T is the absolute temperature, C is the molar concentration of Li^+ ions, A is the electrode area, and F is the Faraday constant. The Warburg impedance coefficient σ_w can be calculated from the slope of the Z_{Re} vs. $\omega^{-1/2}$ plot. The calculated Warburg factors for the Si NPs and Si/SCWAC composite were 50.124 and 13.756, respectively. From Eq. (2), the lower Warburg factor gives a higher diffusion coefficient (D), where the calculated D values for the Si NPs and Si/C electrodes were 5.87×10^{-12} and 7.79×10^{-11}, respectively. The higher D value indicates faster kinetics of the cell reactions at the Si/C electrode owing to the high conductivity and shorter Li^+ and electron transport lengths resulting from SCWAC [33]. The performance of the prepared Si/SCWAC composite was compared with that of previously reported Si/carbon composite anodes, and the results are summarized in Table 1. Overall, the carbonization of biomass SCW using this simple, cost-effective strategy provides an excellent activated carbon material, which can be used as an efficient green carbon addition to Si anodes, where the composite is an effective anode material for LIBs. This approach using biomass

carbon sources (SCW) can be utilized for the construction of highly stable, low-cost energy storage devices.

Table 1. The performance of the prepared Si/SCWAC composite compared with that of previously reported Si/carbon composite anodes.

Composite anode material	Specific discharge Capacity (mAh g^{-1})	No. of cycles	Applied current density (mA g^{-1})	Ref.
Nano Si/KB composite	671	50	750	6
Si/SiO_x/C composites	726	500	100	20
3D Si/C composite	830	100	400	21
Dual yolk-shell structures	956	430	460	22
Si/rGO composite	750	100	50	36
Si@C@CNT@C	1000	100	420	37
SiNPs@AC/OC	1020	200	360	38
Si/coffee waste derived activated carbon composite	1122	100	200	-----

4. CONCLUSION

In summary, spent coffee waste was used as a biomass carbon source to prepare activated carbon to form a composite with silicon nanoparticles. The composite comprising silicon nanoparticles embedded in the spent coffee waste-derived carbon matrix was prepared by a simple annealing approach. When used as an anode material for Li-ion batteries, the prepared composite exhibited excellent electrochemical properties, ascribed to the collective contributions of the silicon nanoparticles and the carbon matrix, which conferred excellent structural stability and electrical conductivity to the composite material. After 100 cycles, the composite delivered a specific capacity of 1122 mAh g^{-1} at 200 mA g^{-1}, and 759 mAh g^{-1} at 3200 mA g^{-1}. Moreover, the silicon-carbon composite showed ten-fold enhanced diffusion of the Li^+ ions compared with the pristine silicon nanoparticles due to the ionic channels in the former electrode material. This study provides insight into the use of biomass carbon sources for Si-carbon composites and carbon coatings on alloy-based anode materials. This approach can be applied in the large-scale production of Si-based anode materials for Li^+ ion storage applications.

ACKNOWLEDGEMENTS
This work was supported by the 2016 Postdoctoral Research Program of Inje University.

AUTHOR CONTRIBUTIONS
Venugopal Nulu designed the experiments, prepared all the samples, characterized them, performed electrochemical measurements, analyzed the results, and drafted the manuscript.

CONFLICTS OF INTEREST
The authors declare no conflict of interest.

References

1. J. M. Tarascon and M. Armand, *Nature*, 414 (2001) 359.
2. M. Armand and J. M. Tarascon, *Nature*, 451 (2008) 7179.
3. G. E. Blomgren, *J. Electrochem. Soc.,* 164 (2017) A5019.
4. J. W. Choi, D. Aurbach, *Nat. Rev. Mater.,* 1(2016) 16013.
5. N. Nitta, F. Wu, J. T. Lee, G. Yushin, *Mater. Today,* 18(2015) 252.
6. N. Arunakumari, N. Venugopal, and K. Y. Sohn, *Sci. Adv. Mater*., 12 (2020), 337.
7. X. Zhou, L. Wu, J. Yang, J. Tang, L. Xi, B. Wang, *J. Power Sources*, 324 (2016) 33.
8. Y. Yu, L. Gu, C. Zhu, S. Tsukimoto, P. A. van Aken, J. Maier, *Adv. Mater.,* 22 (2010) 2247.
9. C. C. Nguyen, S. W. Song, *Electrochem. Commun*., 12(2010) 1593.
10. E. Radvanyi, W. Porcher, E. D. Vito, A. Montani, S. Franger, S. J. S. Larbi, *Phys. Chem. Chem. Phys.,* 16 (2014) 17142.
11. L. Yang, H. S. Chen, H. Jiang, Y. J. Wei, W. L. Song, D. N. Fang, *Chem.Commun*., 54 (2018) 3997.
12. Y. Chen , X. Zhang , Y. Tian and X. Zhao , *J. Nanomater.*, 2014 (2014) 6.
13. W. Liu, H. Xu, H. Qin, Y. Lv, F. Wang, G. Zhu, F. Lin, L. Wang, C. Y. Ni, *J Solid State Electrochem*., 12 (2019) 3363.
14. J. Lee, J. H. Moon, *Korean J. Chem. Eng*., 34 (2017) 3195.
15. A. Nulu, V. Nulu, and K. Y. Sohn, *Korean J. Chem. Eng.,* 37(2020) 1795.
16. M. K. Kim, W. H. Shin, H. M. Jeong, *Appl. Surf. Sci*., 467 (2019) 926.
17. A. Nulu, V. Nulu, and K. Y. Sohn. *ChemElectroChem*, 7(2020) 4055.
18. T. Yang, X. D. Tian, X. Li, K. Wang, Z. J. Liu, Q. G. Guo, Y. Song, *Chem. Eur. J.*, 23(2017) 2165.
19. D. Wang, M. Gao, H. Pan, J. Wang, Y. Liu, *J. Power Sources,* 256 (2014) 190.
20. L. Qian, J. L. Lan, M. Xue, Y. Yu, X. Yang, *RSC Adv.,* 7(2017) 36697.
21. Y. Jiang, S. Chen, D. Mu, B. Wu, Q. Liu, Z. Zhao, F. Wu, *J. Mater. Sci.,* 52(2017) 10950.
22. L. Y. Yang, H. Z. Li, J. Liu, Z. Q. Sun, S. S. Tang, M. Le, *Sci. Rep.*, 5 (2015) 1.
23. W. Y. Long, B. Z. Fang, A. Ignaszak, Z. Z. Wu, Y. J. Wang, D. Wilkinson, *Chem. Soc. Rev.*, 46 (2017) 7176.
24. B. Campbell, R. Ionescu, Z. Favors, C. S. Ozkan, M. Ozkan, *Sci. Rep.,* 5 (2015) 14575.
25. L. P. Wang, Z.Schnepp, M. M.Titirici, *J. Mat. Chem. A*, 1(2013) 5269.
26. P. Zheng, T. Liu, J. Z. Zhang, L. F. Zhang, Y. Liu, J. F. Huang, S. W. Guo, *RSC Adv.,* 5(2015) 40737.
27. C. Kourmentza, C. N.Economou, R. Tsafrakidou, M. Kornaros, *J. Clean. Prod.*, 172 (2018) 980.
28. D. C. dos Santos, M. A. Adebayo, E. C. Lima, S. F. P. Pereira, R. Cataluña, C. Saucier, P. S. Thue, F. M. Machado. *J. Braz. Chem. Soc.*, 26 (2015) 924.
29. A. Kovalcik, S. Obruca, N. Marova, *Food Bioprod. Process,* 110 (2018) 104.

30. K C. Kemp, S. B. Baek, W.-G. Lee, M Meyyappan, K. S. Kim. *Nanotechnology*, 26 (2015) 385602.
31. Y.S.Yun, M.H.Park, S.J.Hong, M.E.Lee, Y.W.Park, H.J. Jin, *ACS Appl. Mater. Interfaces*, 7(2015) 3684.
32. S. M. Kang, M-Seob, K. Y. Jeoun, C. Hudaya, Y.-E. Sung, Bull. Korean Chem. Soc., 40 (2019) 857.
33. D. Y. Chung, Y. J. Son, J. M. Yoo, J. S. Kang, C.-Y. Ahn, S. Park, Y.-E. Sung, *ACS Appl. Mater. Interfaces,* 9 (2017) 41303.
34. K. Kikichi, T. Yasue, R. Yamashita, S. Sakuragawa, M. Sudoh, M. Itagaki. *Electrochemistry*, 81 (2013) 828.
35. H. Yue, S. Wang, Z. Yang, Q. Li, S. Lin, D. He, *Electrochim. Acta*, 174(2015) 688.
36. C. Botas, D. Carriazo, W. Zhang, T. Rojo, and G. Singh, *Appl. Mater. Interfaces*, 8 (2016) 28808.
37. G. Fang, X. Deng, J. Zou and X. Zeng, *Int. J. Electrochem. Sci.,* 14 (2019) 1580.
38. G. Fang, X. Deng, J. Zou, and X. Zeng, *Electrochimica Acta*, 295 (2019) 498.
39. M. Zhou, T. Cai, F. Pu, H. Chen, Z. Wang, H. Zhang, S. Guan, *ACS Appl. Mater. Interfaces*, 5(2013) 3449.
40. A. Gohier, B. Laïk, K. H. Kim, J. L. Maurice, J. P. P. Ramos, C. S. Cojocaru, P. T. Van, *Adv. Mater*., 24 (2012) 19.
41. W. Wang, R. Epur and P. N. Kumta, *Electrochem. Commun.*, 13(2011) 5.
42. A. Nulu, V. Nulu, and K. Y. Sohn. *ChemElectroChem*, 8(2021) 1259.
43. X. Zhou, Y. Yu, J. Yang, H. Wang, M. Jia, J. Tang, *ChemElectroChem*, 6 (2019) 2056.